Mechanical properties and corrosion behavior of HBN and α-Al_2O_{3w} hybrid reinforced laminated Cu matrix composites

Zhijian Li[a,b], Xiaosong Jiang[a,b], Hongliang Sun[a,b], Yong Pang[c*], Zixuan Wu[d], Liu Yang[e]*

[a]Key Laboratory of Advanced Technologies of Materials, Ministry of Education, Chengdu 610031, China

[b]School of Materials Science and Engineering, Southwest Jiaotong University, Chengdu Sichuan 610031, China

[c]School of Materials Science and Engineering, Central South University, Changsha, 410083, China

[d]School of Engineering and Materials Science, Queen Mary University of London, London E1 4NS, United Kingdom

[e]Institute for Applied Materials (IAM-WK), Karlsruhe Institute of Technology (KIT), Karlsruhe 76131, Germany

*Corresponding author: xsjiang@swjtu.edu.cn (X.S. Jiang) OR thgink@126.com (Y. Pang).

Abstract

Inspired by the hierarchical structure of pearl shells and its associated multi-scale toughening mechanism, laminated copper matrix composites reinforced with hexagonal boron nitride (HBN) and α-Al_2O_3 whiskers (α-Al_2O_{3w}) hybridization were successfully prepared by flake powder metallurgy. Results showed that with increase of HBN content, mechanical and corrosion properties of laminated composites were significantly improved. The best mechanical properties and corrosion properties were achieved at the HBN content of 1.5 wt.%. Compared with non-laminated composites,

laminated composites had higher relative density, better strength and toughness, their tensile strength and elongation were increased by 11.01 MPa, 2.57%, respectively. Fibrous α-Al_2O_{3w} can play a crack tip shielding effect, laminated structure of Cu matrix brings a variety of crack deflection modes and increases energy dissipation. Large aspect ratio of Cu flakes in vertical laminated direction brought about a shunting effect that made corrosion difficult to proceed to interior. This work provides new ideas for obtaining Cu matrix composites with high strength, high toughness and good corrosion properties.

Keywords: Laminated composites; Hexagonal boron nitride; α-Al_2O_{3w}; Mechanical properties; Corrosion behavior

1 Introduction

Copper matrix composites, notable for their excellent electrical and thermal conductivity, machinability, and corrosion resistance, find extensive applications in fields like electronics, communications, marine engineering, and aerospace [1,2]. However, with the development of science and technology, the contradiction between strength and toughness of composites has been hindering the application of metallic materials [3]. In recent years, the bionic materials with high strength and high toughness have provided new ideas for the development of composites. For example, pearl layer biological material consists of calcium carbonate as a "brick" and organic protein as a "mud", and they are combined to form similar "brick-mud" structure [4,5], which results in a biomaterial with both high strength and toughness. Luo [6] obtained Cu-α-Al_2O_{3w}-MWCNTs laminated composites by flake powder metallurgy, results showed that large grain size favored dislocation motion in plane, while interlayer interface and nanocrystals prevented the combination of dislocation motion vertical to plane, achieving a balance of strength and toughness. Meanwhile, during the fracture process, the laminated structure changes the crack extension path [7,8], and the deflection of the crack path consumes more energy, thus enhancing the toughness of material. Similarly, Hu et al [9] constructed laminated Cr3C2 between ceramic reinforcement TiC and copper. It was demonstrated that this laminated structure achieved various external toughening mechanisms, such as synergistic plastic deformation of metal and ceramic layers, ductile bridging of metal, and multiple cracking patterns thus achieving high

strength and toughness [6,10,11]. Therefore, it shows a balance of strength and toughness and obtains better mechanical properties. At the same time, special laminated structure also can improve corrosion properties of material. Zhang et al. [12] introduced graphene films into Cu flakes by electrostatic self-assembly. They found that corrosion paths changed from deep vertical development to lateral expansion, and multiple corrosion paths alleviated tendency of corrosion to develop internally. In summary, laminated structure can balance toughness and strength by hindering dislocation movement, and special multi-cracking pattern while changing corrosion path to enhance corrosion properties, which shows great potential in improving properties of material.

In recent studies, flake powder metallurgy [10], preform molding [13], freeze casting [14] have been used to prepare laminated composites. Among them, flake powder metallurgy is more suitable for industrial production due to its high efficiency and degree of freedom. Wei [10] used flake powder metallurgy (FPM) to prepare carbon nanotube-Al laminated composites. The best experimental results were obtained by adjusting ball milling parameters to obtain different thicknesses and widths of Al flakes. Jiang et al. [15] found that flake metal powders had better geometric compatibility with reinforcement, increased adsorption capacity and improved reinforcement dispersion by comparing composites prepared from spherical and flake powders. A plethora of studies indicate that Flake Powder Metallurgy (FPM) can ameliorate interface issues in composites and is applicable in the fabrication of laminated composites.

α-Al_2O_{3w} have a unique fiber structure with excellent properties such as high

strength, high corrosion resistance and high temperature stability. Corrochano et al. [16] reported that α-Al_2O_{3w} have better interfacial contact with metal compared to Al_2O_3 particles. Also, during the fracture process, pull-out and fracture changes of α-Al_2O_{3w} can have a significant hindering effect on crack extension [7,17]. Hexagonal boron nitride (HBN) is the most stable of all crystalline forms of BN, consisting of sp^2 heterogeneous, alternating boron and nitrogen atoms in an atomic ratio of 1:1 in a honeycomb structure [18,19]. The N and B atoms are connected by strong covalent bonds and have a high elastic modulus, and it also has high chemical stability, low density, and high thermal stability [20,21]. In the current research, most of studies use HBN as a lubricating material to enhance the frictional wear properties and mechanical properties of material [22-25]. However, in recent studies, more and more scholars began to pay attention to high chemical stability and thermal stability of HBN [26,27]. For metal matrix composites, a single reinforcement has a limited effect on the reinforcement of matrix, while the mode of co-reinforcement of multiphase reinforcement leads to better overall performance [28-30]. Shao [31] prepared α-Al_2O_{3w} and graphene co-reinforced copper matrix composites. They found that when microcracks at α-Al_2O_{3w}/Cu interface expand along interface, graphene embedded in composites prevents crack expansion and strengthens α-Al_2O_{3w}, thus creating a hybridization enhancement effect. Since HBN and graphene have same two-dimensional structure, based on the principle of hybridization enhancement, two-dimensional HBN and fibrous α-Al_2O_{3w} can be used as reinforcement to achieve better enhancement effect.

In current research, there is limited studies on HBN reinforced laminated Cu matrix composites and the corrosion properties of laminated composites. 2D materials can reduce ring breaking of Cu flakes during the mixing process, thus making better laminated structure [33]. In this study, in order to prepare Cu matrix composites with high strength, toughness and corrosion properties, Cu-HBN-α-Al_2O_{3w} were surface modified by sodium dodecyl sulfate solution, combined with HBN as reinforcement, and Cu-HBN-α-Al_2O_{3w} laminated composites were prepared by FPM and vacuum hot pressing (VHP). The effects of laminated structure and HBN content on microstructure, mechanical properties and corrosion properties of composites were investigated against non-laminated composites, and strengthening, fracture and corrosion mechanisms were studied and discussed in detail. The experimental results showed that the hybrid reinforcement of HBN and α-Al_2O_{3w} as well as the multiscale toughening mechanism of laminated structure balanced the strength and toughness of the laminated composites, and the special laminated structure brings about different corrosion behaviors.

2. Experiment

2.1 Materials

Pure Cu powders (99% purity, 40 μm mean particle size) was used as matrix. HBN (99.9% purity, 4 μm mean particle size), α-Al_2O_{3w} (D: 0.1-4 μm; L: 5-30 μm) were used as reinforcement. The Cu powders and HBN used in this study were provided by Shanghai Naiou Nano Technology Co., Ltd. α-Al_2O_{3w} were provided by Advanced Composites Research Department, Tsinghua Innovation Center, Dongguan, China, and

chemical reagents used in this study were provided by Chengdu Kelong.

2.2. Fabrication of composites

In this study, four composites were prepared, where sample H1 was a non-laminated composites with 0.5 wt.% HBN content and samples H2-H4 were laminated composites with 0.5 wt.%, 1 wt.%, 1.5 wt.% HBN content. 1 wt.% α-Al_2O_{3w} were added to each sample to achieve hybridization enhancement. To obtain Cu flakes, ball milling process was conducted using a ball-milling in stainless-steel ball and a ball-to-powder ratio of 20:1, while tert-butanol was added as a ball milling medium. The spherical Cu powders was ball milled at 300 rpm for 4 h, 6 h, and 8 h, respectively. The surface modification of α-Al_2O_{3w} was performed using sodium dodecyl sulfate under ultrasonic oscillation (KQ-600DE) at a power of 600 W and a frequency of 40 kHz for 20 min, followed by standing for 24 h. The modified α-Al_2O_{3w}, HBN and Cu flakes were weighed and mixed using a planetary ball mill (WL-1) at 300 rpm for 60 min. The powders slurry after ball milling was dried using a vacuum freeze dryer (FD-a-50) for 24 h to obtain composite powders. It was encapsulated in a circular graphite mold with a diameter of 55 mm. The graphite molds were placed in a vacuum hot press furnace (HAS-25) and heated to 850 °C at a rate of 10 °C/min under a pressure of 30 MPa, followed by holding for 60 min. The flow chart of experiment is shown in Fig. 1.

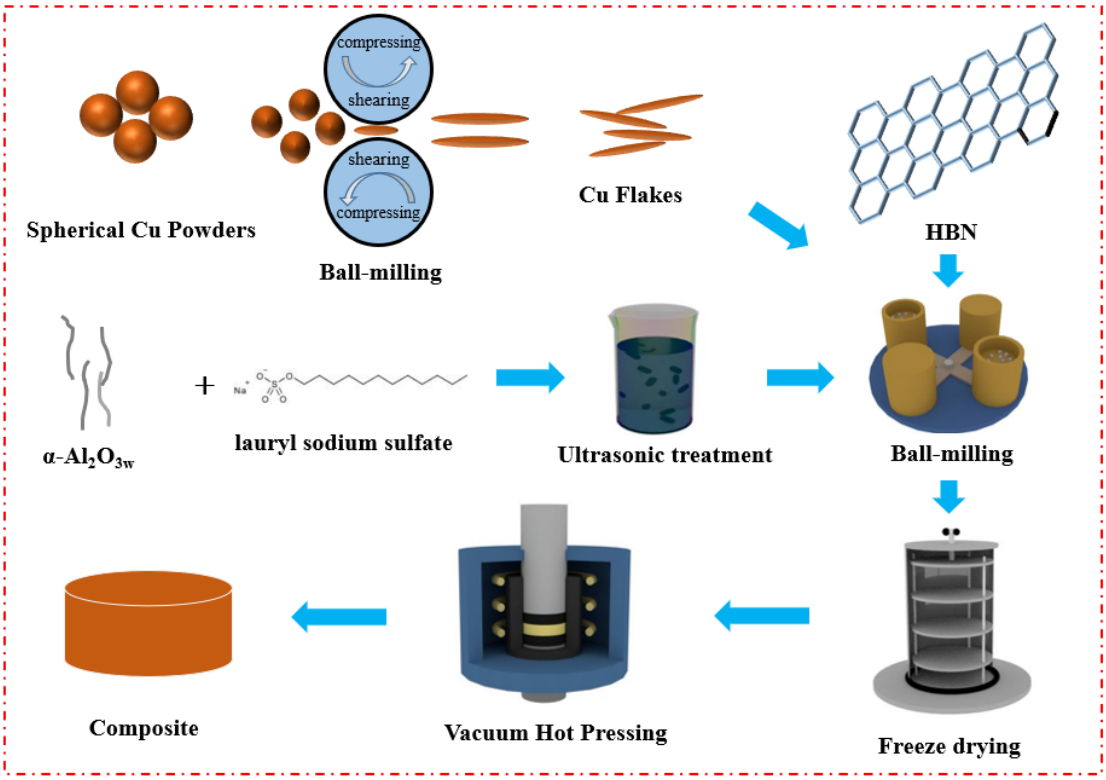

Fig. 1 Schematic diagram of preparation of Cu-HBN-α-Al_2O_{3w} composites

2.3 Characterization of composites

The Archimedean drainage method was used to determine the actual density (ρ) of the four specimens and combined with the theoretical density to calculate the densities of the four specimens. The phase and microstructure of the powders and blocks were analyzed by X-ray diffraction analysis (XRD, X. pert pro-mpd) and scanning electron microscopy (SEM ZEISS Gemini SEM 300) equipped with an energy dispersive X-ray spectroscopy (EDS) detector. Tensile and compressive strengths were measured using a universal testing machine (WDW-3100). The loading rate for tensile and compression tests was 0.5 mm/min. In addition, compression fracture morphology of composites was characterized and studied by SEM (ZEISS Gemini SEM 300)) and EDS in order to investigate the fracture and strengthening mechanisms of composites.

To study the corrosion properties of material, electrochemical workstation (Gamry 1010) was used to perform electrochemical tests. The workstation used a traditional three-electrode system which sample was working electrode, graphite electrode was counter electrode, and saturated glycerol electrode (SCE) was used as the reference electrode. The direction vertical to laminated test was marked as v-direction and parallel to laminated test direction was noted as the p-direction. The test temperature was room temperature and test medium were 3.5 wt.% NaCl solution. To ensure the stability of experiments, the samples were immersed for 1 h before the tests to reach a stable value of open circuit voltage. The scanning range of the dynamic potential polarization curve was ±1 V relative to open-circuit potential at a rate of 5 mV/s. The frequency range of the electrochemical impedance spectroscopy (EIS) test was 0.01 Hz-100 kHz.

3. Results

3.1. Characterization of composite powders

Wider and thinner Cu flakes can bring a larger contact area with reinforcement, thus increasing the contact area of interface obtaining laminated composites with better interfacial bonding [10]. Fig. 2(a-f) shows Cu flakes with different size morphologies obtained after different ball milling times. Fig. 2(a, d) shows the SEM images of Cu flakes after 4 h of ball milling. The diameters of the flakes are 35-45 μm and most of them are above 35 μm, thickness is 1 μm. While after 6 h of ball milling (Fig. 2 b, e), Cu flakes with transverse dimensions above 100 μm and the thickness is below 1 μm. The overall Cu flakes morphology is higher, wider and thinner compared to ball milling

4 h. Severe adhesion leads to severe non-uniformity in the size of Cu flakes. After 8 h of ball milling, the Cu flakes became uniform in size, but smaller in diameter, generally between 15-25 μm. And phenomenon of agglomeration of multiple broken Cu slices appears. The principle of the transformation of Cu powders from spherical to flake is through collision and extrusion of stainless-steel balls [6,33], by the combined effect of shear and compression forces to form flakes. With the increase of ball milling time, the number of collisions increases, generating excess kinetic and thermal energy. It will lead to more serious phenomenon of Cu flakes fragmentation and promote the agglomeration of broken Cu flakes.

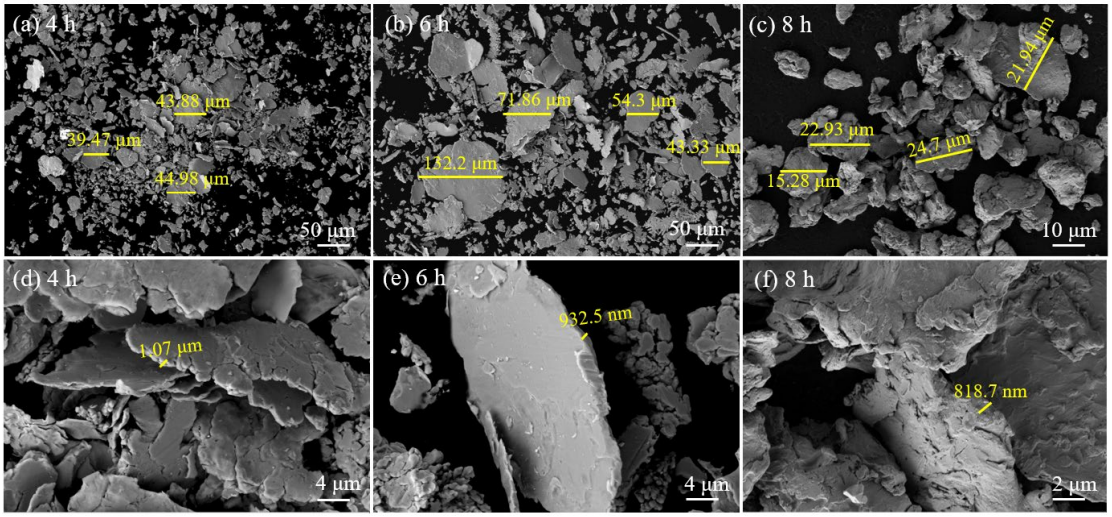

Fig. 2 SEM images of Cu flakes at different ball milling times (a, d) 4 h; (b, e) 6 h; (c, f) 8 h

Fig. 3 shows morphology and EDS plots of 0.5 wt.% HBN laminated and non-laminated composite powders. It is observed that the spherical copper powders remained spherical after mixing, while the laminated copper powders remain undamaged and flaky after mixing. Meanwhile the diameter of Cu flakes after mixing is between 30 μm and 50 μm, while the pure Cu powder after 6h of ball milling has a

larger diameter. This may be related to the breakdown of Cu flakes during 1h of mixing. Fig. 3(c, d) shows the distribution of the local reinforcement. The spherical Cu powders has poor contact with reinforcement, but HBN is embedded or laid flat on the laminated Cu powders. The large lateral size of Cu powders provides a larger contact area for self-assembly with reinforcement during ball milling, which not only distributes reinforcement uniformly in the matrix, but also facilitates the formation of the laminated structure. The results show that the flake powders obtained by ball milling for 6 h has better geometric compatibility, which promotes the uniform distribution of reinforcement and formation of the laminated structure.

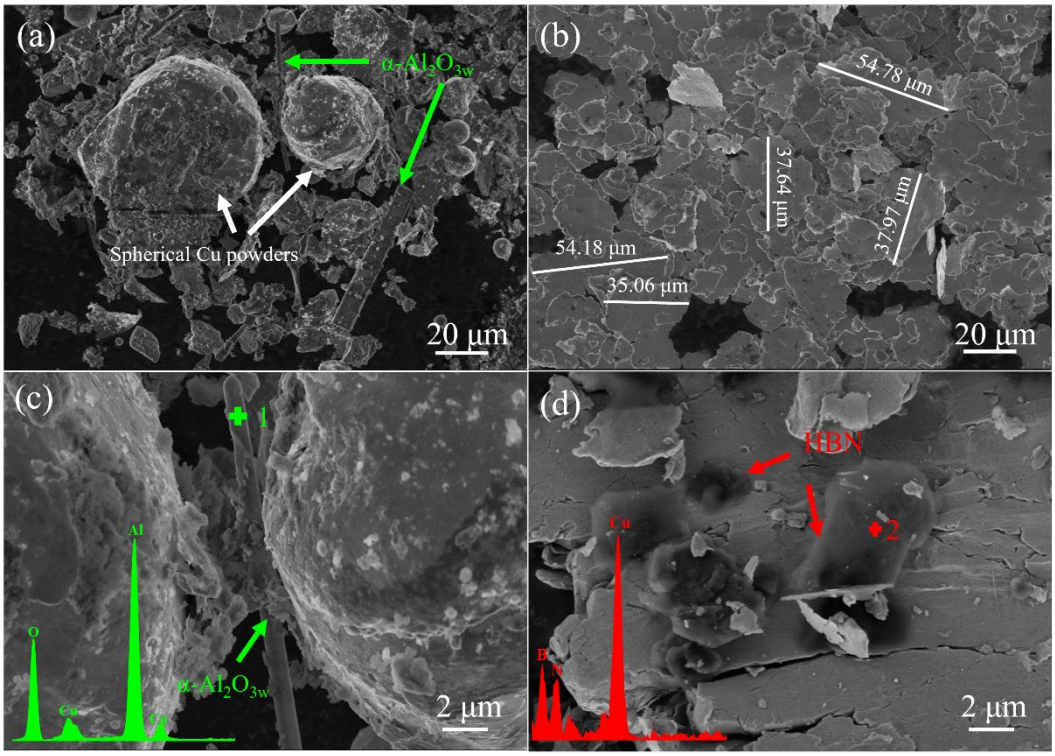

Fig. 3 Cu-0.5wt.%HBN-0.5wt.%α-Al_2O_{3w} (a, c) non-laminated powders; (b, d) laminated powders SEM and EDS

3.2 Characterization of the sintered composites

Fig. 4 shows the cross-sectional microstructure of composites, where the black area is reinforcement and the gray area Cu. Fig. 4(a) is non-laminated composites, while fig. 4(b-d) are laminated composites. In comparison, reinforcement distribution is more disordered in the non-laminated structure in Fig. 4(a), while reinforcement appear to be parallel oriented in Fig. 4(b-d). Meanwhile, with the increase of HBN, composites with HBN content of 1 wt.% and 1.5 wt.% showed obvious laminated structure. With the increase of HBN content, the laminated structure is gradually clear, and the composites with HBN content of 1.5 wt.% have the best laminated effect. From the surface SEM results, HBN and α-Al_2O_{3w} show a clear laminar structure in the composites prepared by FPM.

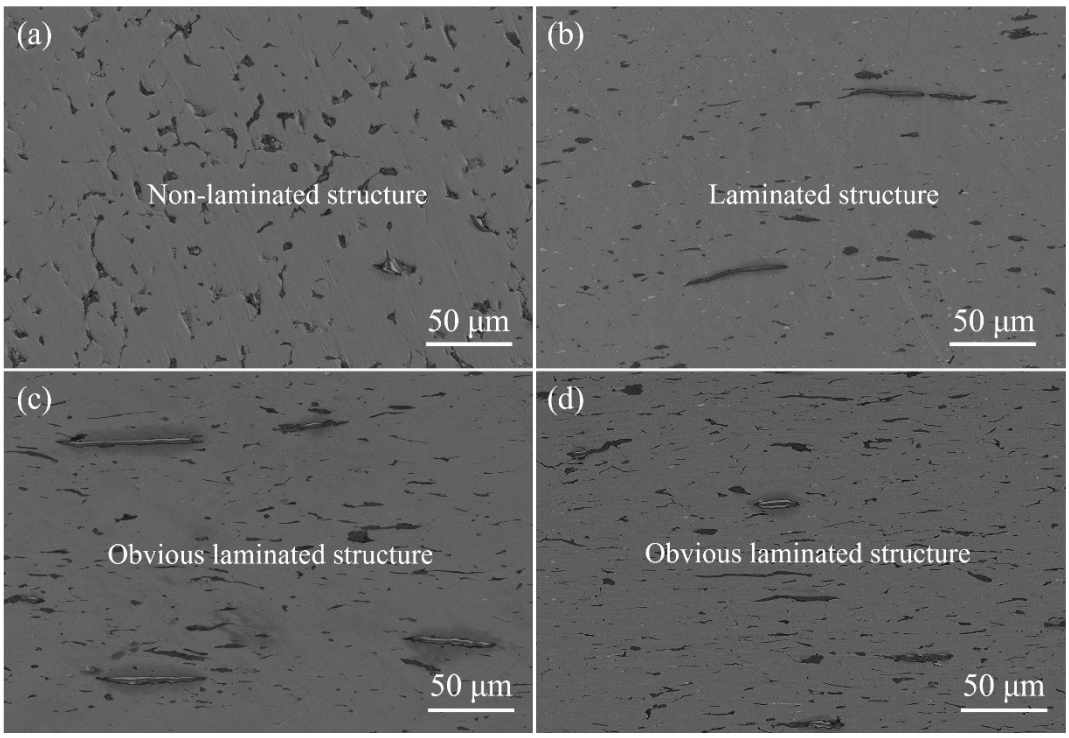

Fig. 4 SEM images of composites (a) H1; (b) H2; (c) H3; (d) H4

In order to better distinguish the distribution of reinforcement, EDS is performed on materials and the results are shown in Fig. 5. It shows EDS plots of the laminated composites with 1.5 wt.% HBN content. The distribution of HBN can be seen in Fig. 5(b, c), which shows a trend of uniform dispersion of HBN, and the laminated structure is not obvious. However, Fig. 5(d, e) shows that α-Al_2O_{3w} has a large transverse size in the matrix, which shows an obvious laminated structure. The reason for this phenomenon is related to the properties of both materials. First of all, HBN has a smaller transverse dimension and lacks free electrons and weak metal bonds due to weak van der Waals forces between BN layers, which results in high ionic bonding rates [23]. This makes HBN more strongly adsorbed with matrix, and the strong force between stainless-steel ball and powders during ball milling process can form a mechanical bond between reinforcement and the Cu flakes to achieve mechanical self-assembly effect [6,7]. The excellent dispersibility and relatively small lateral dimensions of hexagonal boron nitride (HBN) allow for its uniform dispersion within the matrix, thereby rendering its layered structure less conspicuous. In contrast, α-Al_2O_{3w} can show a more significant laminated structure in composites due to its special fiber-like structure with larger transverse dimensions. The results show that α-Al_2O_{3w} shows a better laminated structure in composites, while HBN is uniformly distributed in matrix.

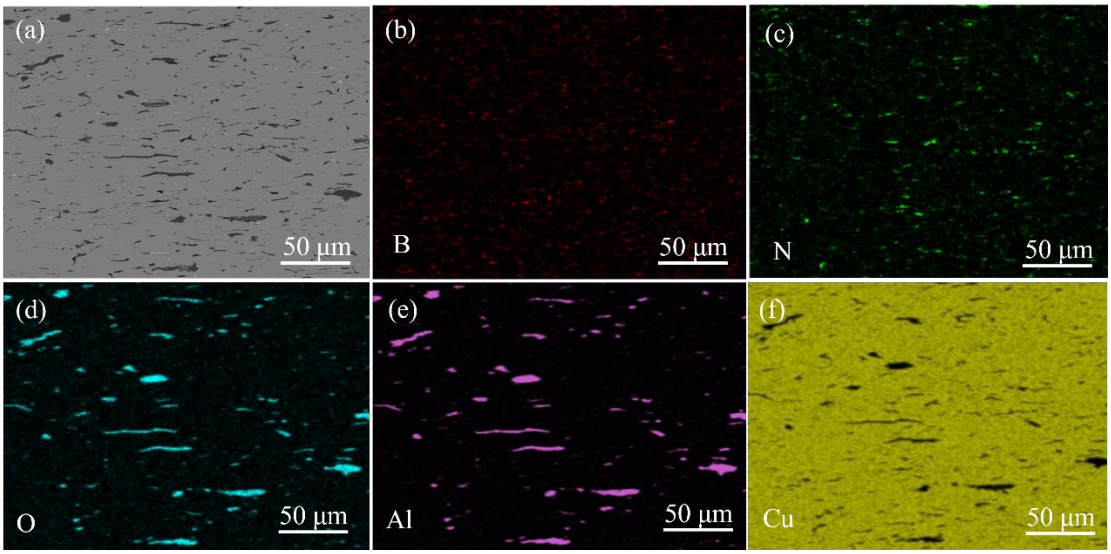

Fig. 5 EDS map of laminated composites (a) laminated composites Cu-1.5 wt.% HBN-0.5%α-Al_2O_{3w}; (b) distribution of B; (c) distribution of N; (d) distribution of O; (e) distribution of Al; (f) distribution of Cu

Fig. 6 shows XRD pattern of powders and composites. The analysis revealed that characteristic peaks of Cu and HBN were exclusively observed in both the powder and composites, with the absence of α-Al_2O_{3w}. It is hypothesized that the non-detection of α-Al_2O_{3w} may be due to their low concentration. Additionally, no extraneous impurities are detected in the results. This implies that no contaminants were introduced during the ball milling and sintering processes, and no reactions occurred during the sintering phase. The diffraction angles of Cu peaks in sintered composites are around 43.329, 50.402°and 74.071°, respectively, while HBN and Cu matrix are in same peak position. The crystallographic indices of Cu are (111), (200) and (220), while those of HBN are (200) and (220) from left to right. Fig. 6(c) shows XRD comparison of powders and block of Cu-1.5 wt.% HBN-1 wt.% α-Al_2O_{3w} composites. The angle of 45°-55° is selected for further highlighting the comparison, as in Fig. 6(d). Taking the peak on

(200) crystal plane as an example, the peak on the (200) plane of composites is slightly broadened and height side is short. It indicates a grain refinement of material after sintering, which is related to refinements caused by the addition of HBN [25,33].

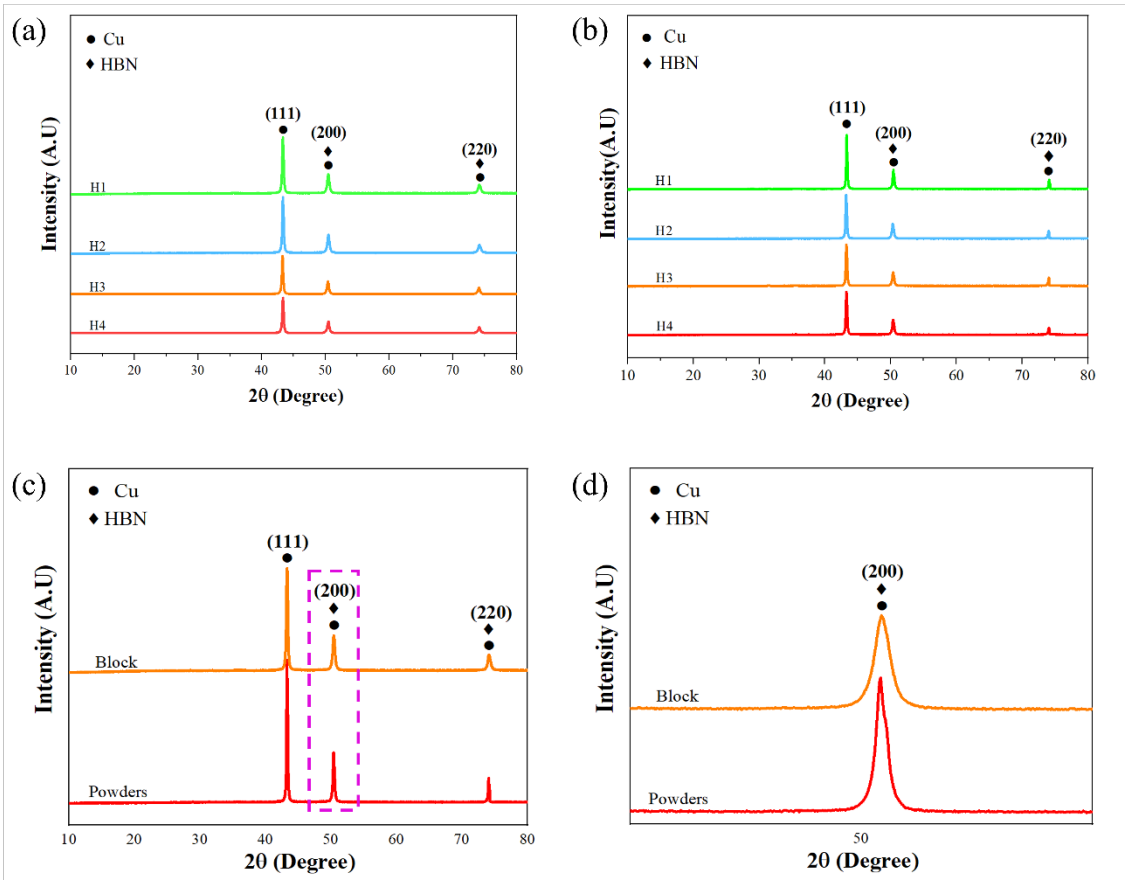

Fig. 6 XRD patterns of composites: (a) powders; (b) composites; (c) comparison of block and powders of 1.5 wt.% HBN; (d) enlarged view of the marked area

3.3 Mechanical properties analysis of composites

Archimedes principle is used to measure the density of laminated composites, actual density of HBN, α-Al_2O_{3w} were 2.1 g/cm^3, 3.99 g/cm^3 [31,32]. The actual densities of composites are calculated as 8.59 g/cm^3, 8.59 g/cm^3, 8.32 g/cm^3, 8.06 g/cm^3.

The results show that the densities of all materials are higher than 98.49% and completely dense. Comparing laminated and non-laminated composites, the densities of laminated composites are higher, which is caused by the increased contact area of Cu flakes with reinforcement compared with spherical Cu powders [33]. The greater contact area reduces voids between matrix and reinforcement during sintering, resulting in higher densities. The density of the composites tends to decrease as the HBN content increases. This is due to the fact that as the amount of the reinforcement increases, agglomeration occurs in the matrix, and voids at agglomeration sites make it difficult to fill the gaps during the sintering process, leading to the formation of internal defects. However, the density of the composites containing 1.5 wt.% HBN still reached 98.49%, which indicates that the laminated composites is successfully prepared.

Tensile and compression tests are performed on each sample. The tensile direction was parallel to ply direction and the compression direction was vertical to ply direction. The results are shown in Table 1 and Fig. 7. Fig. 7(a, b) shows the tensile and compression curves of materials, respectively. Firstly, tensile strength of laminated composites is increased by 11.01 MPa, the elongation is increased by 2.57% and compressive strength is increased by 82.13 MPa compared with non-laminated composites. In the laminated structure, large grain size in the plane of the lamellar is more favorable to dislocation movement, while the interlayer interface and nano-grains in the vertical direction hinder the dislocation movement in the direction vertical to plane. These types of dislocation movement effectively alleviate stress concentration phenomenon and achieve multiple deflections of cracks during fracture [6,34]. So,

composites with laminated structure show better mechanical properties. Subsequently, the mechanical properties and curve changes of laminates with different HBN content were compared. The results show that material tensile and compressive strengths continue to increase with increasing HBN content, but material elongation decreases. The strength of material reached 251.44 MPa at 1.5 wt.% HBN content. Although the elongation decreased, it was still higher than that of non-laminated composites. Due to the impediment of dislocation movement by the laminated structure, and the deflection of cracks during the fracture process consuming more energy, composites with a laminated structure exhibit enhanced tensile and compressive properties.

Table 1 Densities and mechanical properties of composites

Sample	Relative density (%)	Tensile strength (MPa)	±Error (MPa)	Tensile elongation (%)	Compressive strength (MPa)	±Error (MPa)
H1	98.23±0.09	183.23	±6.61	10.68	339.34	±4.47
H2	98.82±0.07	194.24	±2.64	13.25	421.47	±2.8
H3	98.75±0.13	229.16	±6.33	13.11	485.13	±3.5
H4	98.49±0.11	251.44	±2.83	12.59	495.56	±4.26

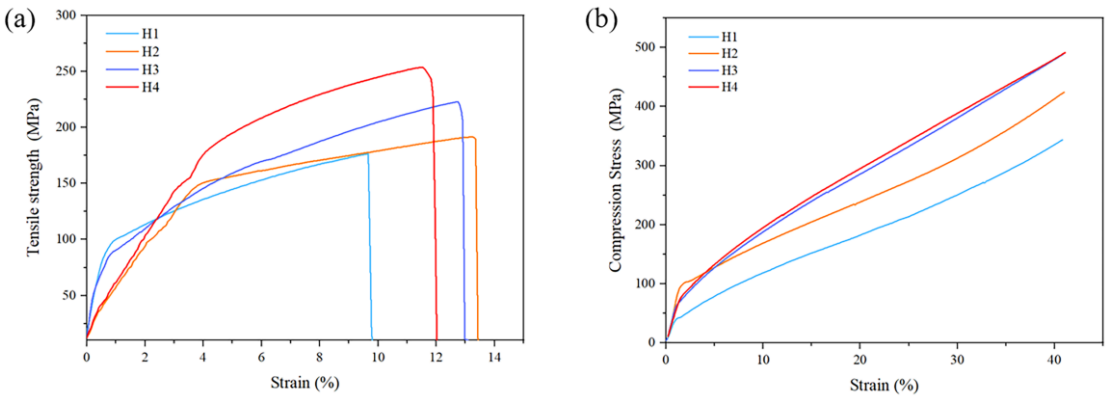

Fig. 7 (a)Tensile stress-strain curve; (b) compressive stress-strain curve of Cu-HBN-α-Al_2O_{3w} composites

Fig. 8 shows SEM of the tensile fractures of laminated composites. All materials show obvious tough nests, which proves that composites are ductile fracture. Fig. 8(a, b) shows tensile fractures of non-laminated composites and laminated composites with same HBN content, respectively. The results show that the fracture in Fig. 8(b) shows a clear laminated structure, whereas the fracture in Fig. 8(a) does not appear to be laminated. It proves that laminated composites were prepared successfully. The fracture patterns of the laminated composites are shown in Fig. 8 (b-d). It can be observed that in addition to tough nests, fracture shows some pits which are caused by the pull-out of α-Al_2O_{3w} or HBN [6,25]. In Fig. 8(c), fragments of HBN can be observed. This is the tearing phenomenon of HBN during the fracture process, and the tearing phenomenon is an important manifestation of the reinforcing effect of reinforcement. The pullout of the reinforcement also leads to cracking at the interface between the reinforcement and the matrix, which leads to crack deflection and bridging. Crack deflection and bridging allow the material fracture force to be uniformly distributed in matrix to avoid sudden fracture due to localized stress concentration [34, 35, 36]. For composites fracture with different HBN contents, the laminated structure of composites gradually becomes blurred with the increase of HBN content. This is due to that the addition of a large amount of reinforcement squeezes the space of the Cu flakes and causes some damage to laminated structure of material [37]. The composites fracture results show that the laminated composites fracture shows a clear laminated structure, and the reinforcement shows two types of reinforcement: pullout and tearing. Multiple reinforcement modes can bring better mechanical properties to matrix. However, with the increase of

reinforcement, the laminated structure of matrix shows signs of destruction.

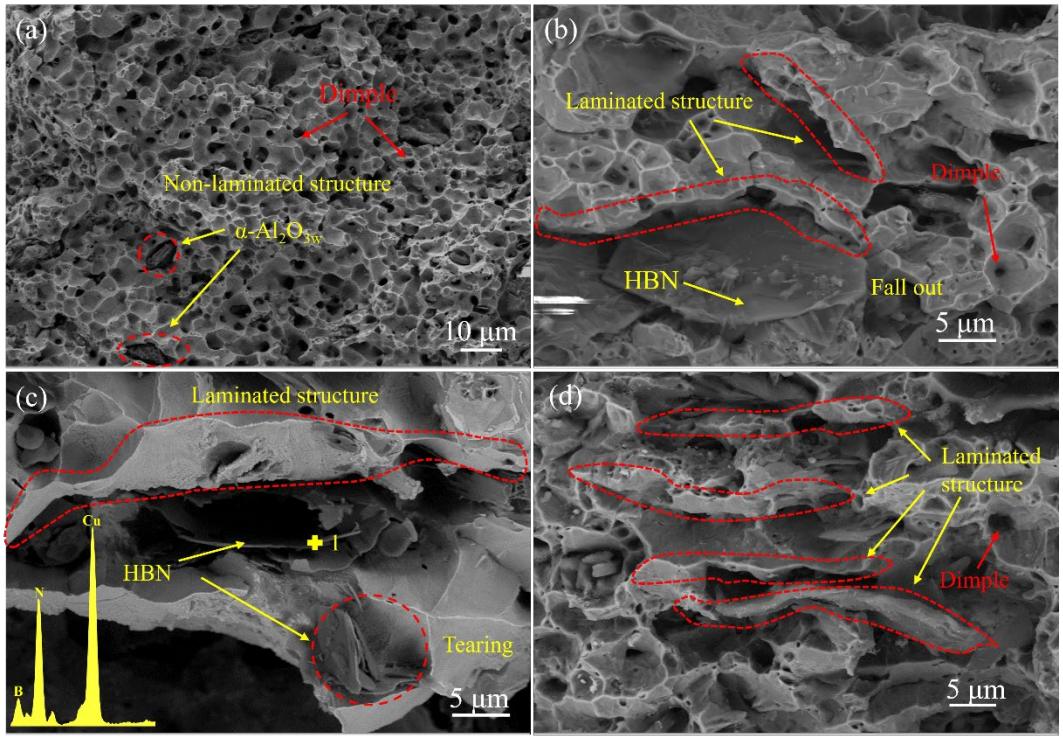

Fig. 8 Tensile fracture SEM of Cu-HBN-α-Al_2O_{3w} composites (a) H1; (b) H2; (c) H3; (d) H4

3.4 Corrosion behavior analysis of composites

Fig. 9 shows Tafel curves of composites under 3.5 wt.% NaCl solution. The curves are divided into cathodic and anodic regions. The Tafel curves show that there is no significant passivation of composites. The electric potential is in region of -0.3 V~-1.3 V for the cathode region. Where -0.3 V~-1.1 V is controlled by the diffusion of dissolved oxygen diffusion [38]. The oxygen uptake reaction occurs at this stage. During the -1.1V to -1.3V phase, the oxygen and hydrogen ion content of solution is depleted, resulting in hydrogen precipitation reactions. The anode region is from -0.3 V to 0.9 V. Where -0.3 V~0 V for the polarization of composites, composites began to

corrosion reaction at this stage. 0 V~0.2 V for the transition zone, corrosion products at this stage in surface accumulation. The figure shows that with increase of HBN, corrosion potential gradually decreases, while corrosion current is also gradually reduced. Meanwhile, laminated composites have a lower i_{corr} than non-laminated composites, only 8.6089 exp-6. Table 2 is the data of corrosion properties obtained by fitting. Where R_p is polarization resistance, η is corrosion inhibition rate, and CR is corrosion rate. The polarization resistance indicates the magnitude of corrosion resistance at the onset of corrosion, while CR and η directly reflect corrosion resistance. Where CR and η are obtained by calculation. The calculation formula is as follows [13,39]:

$$\text{CR=K } I_{corr}\ E.W./d \tag{1}$$

$$\eta = (I_{corr(copper)} - I_{corr(compsites)})/(I_{corr(copper)} \tag{2}$$

In Eq. 1, the unit of CR is myp; K is a constant taken 12.88×10^5. The unit of i_{corr} is mA/cm^2; E.W. is the equivalent in gm; d is the density in gm/cm^3. In Eq. 2 its $i_{corr(copper)}$ for pure copper corrosion current density, $i_{corr(compsites)}$ for composites corrosion current density, find literature get corrosion current density of pure copper is 12.799 exp-6 A/cm^2 [37]. Tafel results show that the corrosion properties of laminated composites are superior to non-laminated composites. The corrosion rate of laminated composites is reduced by 0.01163 mpy. The corrosion inhibition efficiency of the matrix is increased by 17.81%. It's due to special structure of laminated composites. As HBN content increases, the corrosion potential of composites decreases and corrosion tendency increases, but CR decreases. The decrease in E_{corr} is due to increase in the

number of corrosion active sites caused by increase in defects [40]. Combined with data in Fig. 9(b) and Table 2, the corrosion rate of laminated composites in different corrosion directions are differences. The vertical direction is higher than parallel direction. The difference corrosion properties in different corrosion directions of laminated structure was also demonstrated in Zhang's study [12].

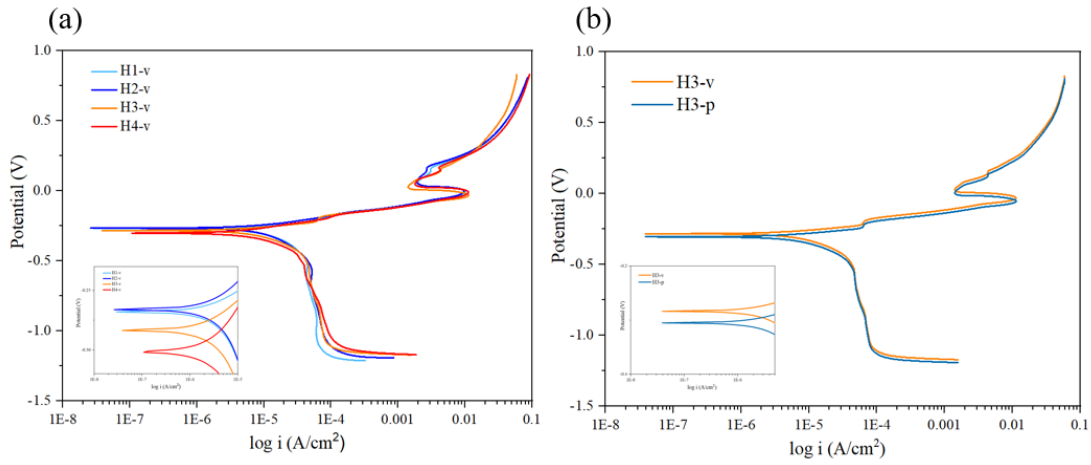

Fig. 9 Polarization curves of (a) different HBN contents in 3.5 wt.% NaCl solution; (b) 1 wt.% HBN composites in different directions

Table 2 Polarization curve fitting results for composites in 3.5% NaCl solution

Sample	i_{corr} (A/cm^2)	E_{corr} (mV)	R_p (Ω)	η (%)	CR (mpy)
H1-v	10.924exp-6	-0.27034	2387.9	15.96	0.05259
H2-v	8.6089exp-6	-0.26724	3030.2	33.77	0.04096
H3-v	7.3467exp-6	-0.28464	3550.8	43.48	0.03496
H4-v	5.963exp-6	-0.30186	4374.8	54.13	0.02941
H3-p	8.0261exp-6	-0.30768	3250.3	38.26	0.03864

EIS can be used to characterize electrochemical reactions and corrosion product formation at metal/electrolyte interface. The impedance spectra are usually displayed as Nyquist plots and Bode plots. Fig. 10 shows EIS plots for four composites with the

test direction in the vertical direction. Also, in order to quantify electrochemical behavior in relation to dynamic behavior, the EIS data were simulated using an equivalent circuit. The fitted circuit is shown in Fig. 10(d). In equivalent circuit, the R_s is solution resistance, CPE1 is constant phase angle progenitor, R_t is charge transfer resistance, and fitted data are shown in Table 3. Overall, it appears that all three materials exhibit high frequency single capacitive resistance arcs and diffuse impedance in low frequency phase. Capacitive resistance value represents material corrosion reaction at beginning of material surface double electric layer on corrosion reaction in degree of charge transfer hindrance [38]. The radius of semicircle and R_t increased with increase of HBN in this experiment. it indicates that the addition of HBN strengthens the corrosion resistance of composites surface. It is worth noting that laminated and non-laminated composites are significantly different with charge transfer resistance values of 153.5 $\Omega.cm^{-2}$ and 881.8 $\Omega.cm^{-2}$, respectively. A larger value of R_t would represent an increase in charge transfer resistance during corrosion and a decrease in corrosion reaction rate. This is same conclusion drawn from Tafel curve. Fig. 10(c) shows Bode plot and each impedance plot shows a gradual increase in impedance with HBN content (log values from 1.9 to 3.6). This suggests that the HBN isolates the corrosion fluid from matrix, thus reducing the corrosion rate. According to Bode plots, the maximum peak angle in the high frequency region can be attributed to increase in HBN reducing the corrosion active sites on surface. The phase angle is constant in low and medium frequency region, the appearance of a constant phase appears CPE properties, probably due to defects on surface [41]. The appearance of

Warburg impedance proves that corrosion products have been generated on composites surface. This stage of corrosion reaction resistance gradually changed from charge transfer control to diffusion control. It is worth noting that Warburg impedance in Table 3 is result of joint action of cathode and anode, and cannot distinguish between two specific gravity [42]. Fig. 11 shows EIS plots of 1 wt.% HBN laminated composites in different directions. In Table 3, the comparison shows more clearly that laminated composites have higher electron transfer resistance in vertical direction and are more resistant to corrosion. The conclusions obtained and Tafel curves prove that for laminated structure, difference in corrosion resistance in different directions is obvious.

From the experimental results, the corrosion properties of composites with laminated structure are significantly better than non-laminated composites. The increase of HBN content can also bring better corrosion properties. At the same time, due to the laminated structure, corrosion properties of composites differed significantly in vertical and parallel laminated directions, and corrosion resistance in vertical direction is better.

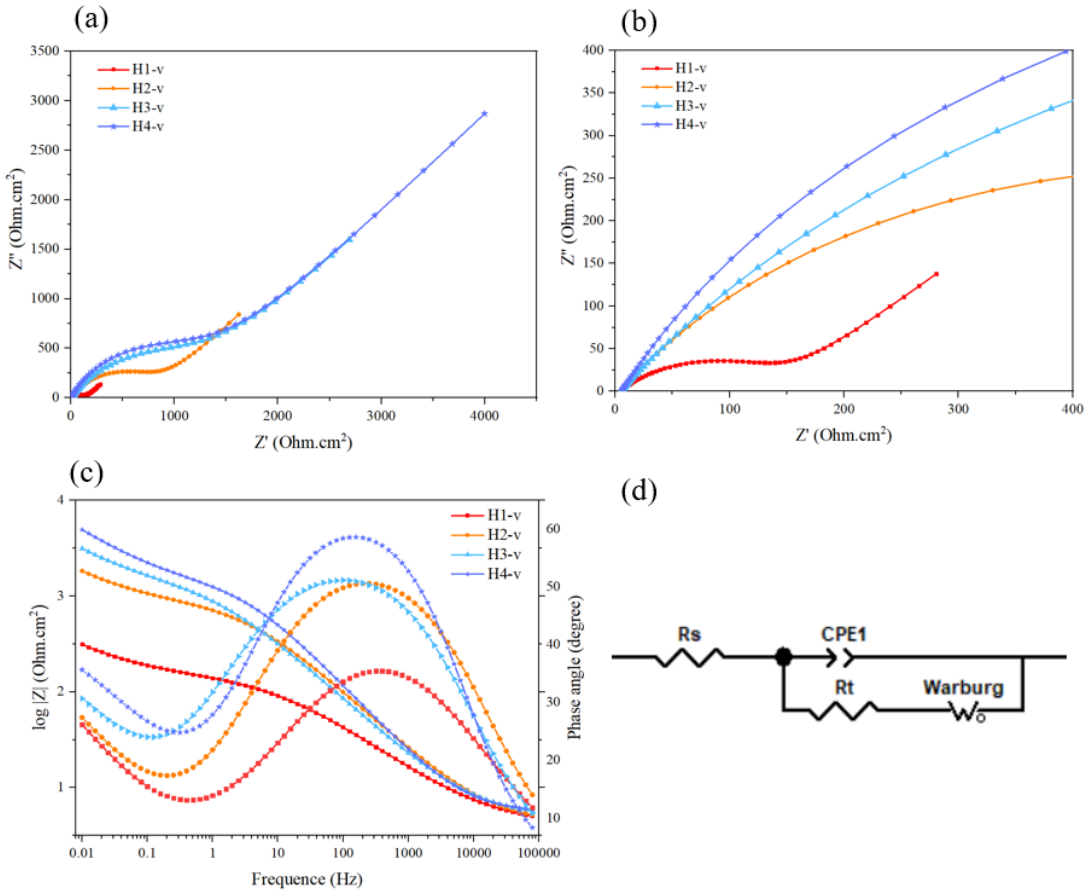

Fig. 10 Composites with different contents HBN in 3.5 wt.% NaCl solution (a) Nyquist plot; (b) Nyquist local magnification; (c) Bode plot; (d) equivalent circuit diagram

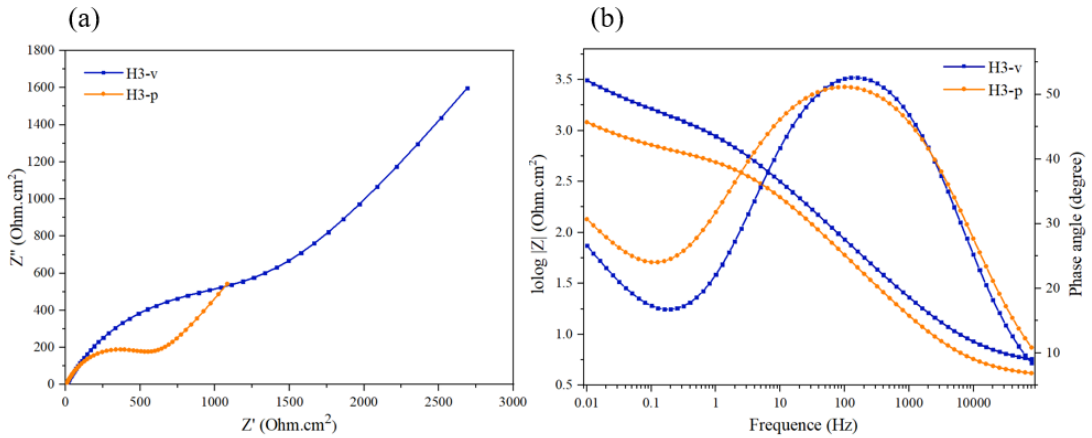

Fig. 11 Different orientations of 1 wt.% HBN laminated composites in 3.5 wt.% NaCl solution (a) Nyquist plots; (b) Bode plots

Table 3 EIS fitting results for composites in 3.5% NaCl solution

Sample	R_s ($\Omega.cm^{-2}$)	CPE1-T	n	R_t ($\Omega.cm^{-2}$)	Warburg (ohm/cm^{-2})
H1-v	3.986	684.4 exp-6	0.523	153.4	20.25 exp-3
H2-v	4.215	164.2 exp-6	0.63	881.8	3.378 exp-3
H3-v	5.467	181.52 exp-6	0.72	1380	975.1 exp-6
H4-v	4.899	206.1 exp-6	0.64	1470	1.752 exp-6
H3-p	3.767	220.7 exp-6	0.67	596.1	5.267 exp-3

4 Discussion

4.1 Strengthening and fracture mechanisms of composites

For laminated composites, the strengthening mechanisms are loading transfer, fine grain strengthening and dislocation strengthening respectively [33,43]. XRD shows that sintered material has a grain refinement. It is caused by the inclusion of reinforcement that hinder growth of grains [25,44]. According to the Hall-Petch relationship, grain refinement can bring better mechanical properties to matrix. The fracture of composites is divided into ductile fracture of matrix and brittle fracture of reinforcement. Fig. 12 illustrates the fracture mechanism of composites. Fig. 12(a, b) shows fracture mechanism of non-laminated structure. The reinforcement is irregularly distributed among matrix and cracks appear in material as load increases. When crack extends to reinforcement position, the shear stress is transferred from interface position of composites to reinforcement. The load transfer phenomenon allows reinforcement to share part of matrix energy and hinder crack extension [45,46]. As the load increases, HBN and α-Al_2O_{3w} will pull out. The pull-out of reinforcement reduces stress concentration and consumes energy at fracture. When reaches ultimate load, the tearing

of reinforcement occurs. The pull-out and tearing of reinforcement during fracture consumes energy of fracture process, thus improving mechanical properties. Shear hysteresis theory is a commonly used model to evaluate transfer of load from matrix to reinforcement [47,48]:

$$\Delta\sigma_{LT} = f\Delta\sigma_m S/2 \quad (3)$$

Where $\Delta\sigma_{LT}$ is the additional reinforcement due to load transfer, f is the volume fraction of reinforcement, $\Delta\sigma_m$ is the yield strength of the pure copper. S is reinforcement aspect ratio. As for laminated composites (Fig. 12 c, d), the strengthening and toughening mechanisms are related to failure mechanism. In the shear hysteresis model, the critical aspect ratio (S_c) that determines the above failure modes is as follow [47-49]:

$$S_c = \sigma_p/\tau_y \quad (4)$$

Where σ_p is the tensile strength of reinforcement, and τ_y is yield shear strength of Cu. When actual aspect ratio of reinforcement is greater than critical aspect ratio ($S>S_c$), reinforcement is brittle fracture failure. While ($S<S_c$), reinforcement is pulled out and fails, at which time material exhibits good toughness. According to the fracture of the composites (Fig. 8), both HBN tearing and HBN pulling were present in the fracture. This also proves that there are two modes of reinforcement failure, one is energy dissipated by brittle fracture of reinforcement itself, and the other is dissipation by interfacial debonding and subsequent friction after reinforcement is pulled out [6,31]. The HBN and α-Al_2O_{3w} with small aspect ratios contribute to the strength toughness of composites mainly through pull-out mode during fracture, while reinforcement with

large aspect ratios enhance material strength by fracture [11,50]. Meanwhile, for laminated composites, during fracture process of laminated composites, initial cracking occurs in a tilted direction. When the crack extends to the position of reinforcement, crack deflects at the position where bond between layers is weak and is forced away from initial plane as in Fig. 12(c, d). The deflection of crack consumes energy at fracture to a greater extent so that composites get better balance of strength and toughness. The crack deflection brings about multiple stress states between interfaces. In previous study, multiple stress states at interface were recorded [8,33], namely: Type I (tensile/opening), Type I/II (tensile/in-plane shear) mixed mode and Type I/III (tensile/anti-plane shear) mixed mode. The mixture of multiple stress states causes crack expansion to show multi-directional deflection. So, the driving force required for crack propagation is higher and energy consumed is higher, which achieves purpose of strengthening and toughening. A variety of strengthening and toughening mechanisms bring superb synergy of strength and toughness for composites.

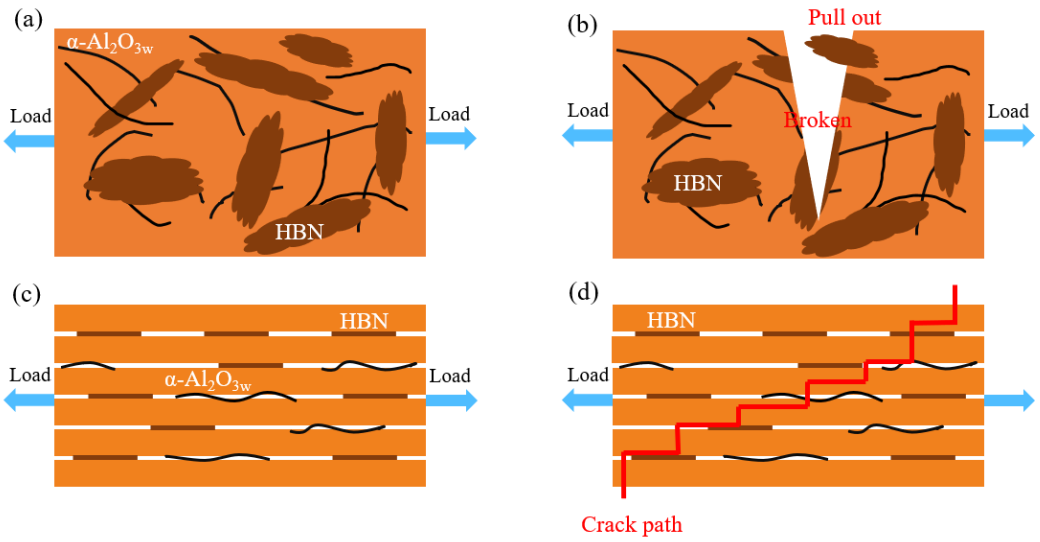

Fig. 12 (a, b) Fracture mechanism diagram for non-laminated composites (c, d)

facture mechanism diagram for laminated composites

4.2 Corrosion mechanism of composites

The mechanism of Cu dissolution in NaCl solutions is understood. In neutral solutions, the cathodic process is mainly an oxygen absorption reaction, and when the oxygen content decreases, hydrogen evolution reaction occurs [51], while the copper keeps acting as an anode. During dissolution process, Cu is first oxidized to Cu^+ (Eq. 5) and then Cu^+ combine with Cl^- in solution to form CuCl (Eq. 6). This stage then corresponds to polarization process in Fig. 9. Since CuCl is a porous film, the corrosion reaction is largely unaffected. As the reaction proceeds, CuCl can continue to combine with Cl^- to form soluble $CuCl_2^-$ (Eq. 7). But $CuCl_2^-$ is unstable phase, and as product builds up $CuCl_2^-$ higher than equilibrium concentration then Cu_2O is formed (Eq. 8), this transition occurs mainly in inner layer in contact with Cu [51,52]. The results in the formation of a dense protective layer inside composites, which forms an internal and external double layer of corrosion products on Cu surface. Cu_2O is a dense oxide film and is key to corrosion resistance of Cu [53]. Due to presence of inner dense corrosion product, the electrode reaction rate is affected by the rate of diffusion of oxygen through corrosion products and Helmholtz layer, which reduces the corrosion current of the composites. This stage corresponds to transition zone of polarization curve in Fig. 9. The dissolution process of Cu in NaCl is as follows [15,38,51]:

$$Cu \rightarrow Cu^+ + e^- \quad (5)$$

$$Cu^+ + Cl^- \rightarrow CuCl \quad (6)$$

$$CuCl+Cl^- \rightarrow CuCl_2^- \quad (7)$$

$$2CuCl_2^-+2OH^- \rightarrow Cu_2O+H_2O+4Cl^- \quad (8)$$

$$O_2+2H_2O+4e^- \rightarrow 4OH^- \quad (9)$$

The EIS of composites proves that composites show significant CPE characteristics. CPE is a special capacitive element whose value is a function of the angular frequency ω and phase is independent of frequency. Its conductance and impedance components are as follows [38,41,42]:

$$Y_{CPE} = Y_0(j\omega)^n \quad (10)$$

$$Z_{CPE} = 1/Y_0(j\omega)^n \quad (11)$$

Where j is an imaginary number, $j = (-1)^{1/2}$, ($\omega=2\pi f$) represents angular frequency and n is power of the CPE, whose magnitude reflects capacitive characteristics of composites. The n is a variable parameter. When n=1, it indicates that material is an ideal capacitor. When n=0, material is an ideal resistor. When 0<n<1, its magnitude describes the extent to which material deviates from the ideal capacitance and resistance [25,38]. The reason for the deviation of n is related to the defects on the surface of composites. The magnitude of the CPE value was experimentally shown to be related to surface roughness and porosity of composites. Jorcin [41] et al. demonstrated that appearance of CPE behavior is closely related to different of charge transfer resistance and interfacial capacitance in different regions of electrode surface by local electrochemical impedance spectroscopy. Therefore, the flatness of surface can be judged by the magnitude of CPE. According to this principle, combined with the results of the EIS fitting, it can be seen that laminated composites have fewer surface defects

and higher flatness than the non-laminated composites. And as HBN content increases, the n decreases and surface integrity of composites decreases, which also leads to more defects on the surface of material. However, more HBN reduces area of Cu exposed to corrosive solution. The insulating reinforcement does not corrode electrically, allowing it to function better as a physical barrier [53,54], reducing corrosion rate and allowing corrosion properties to be enhanced.

Fig. 13 shows corrosion mechanism of laminated composites. The electrochemical results show that corrosion properties of laminated composites are better than non-laminated composites. It is mainly due to special structure. When NaCl solution enters composites after corrosion reaction starts, it will diffuse between layers or at interface. This leads to a dispersion of corrosion path, resulting in multiple branched paths and a change in the diffusion path of ions in the solution [12,39], as shown in Fig. 13(a). The appearance of branched paths leads to a reduction in the corrosion depth of material, with large and shallow pitting pits in laminated composites (Fig. 12), reducing tendency to progress to interior of material. For laminated composites, anisotropy of laminated structure led to significant differences in polarization curves and impedance profiles in transverse and longitudinal directions (Fig. 9, 11). The corrosion current and polarization resistance in vertical direction is higher than those in parallel direction. This is related to large horizontal area in vertical direction, which is prone to corrosion path deviation [15,54], as shown in Fig. 13(b, c). Meanwhile, Jin et al [55] found that parallel to the laminated direction has a larger contact angle, which makes it easier for the external solution to penetrate into material by testing water contact angle in different

directions. The interface between reinforcement and matrix is mechanically bonded, so there is less resistance to the transfer of corrosive solutions to interface. It also provides favorable conditions for corrosive solutions to flow between the interfaces, such as internal flow and ionic diffusion. Therefore, composites exhibit lower corrosion properties in parallel test directions.

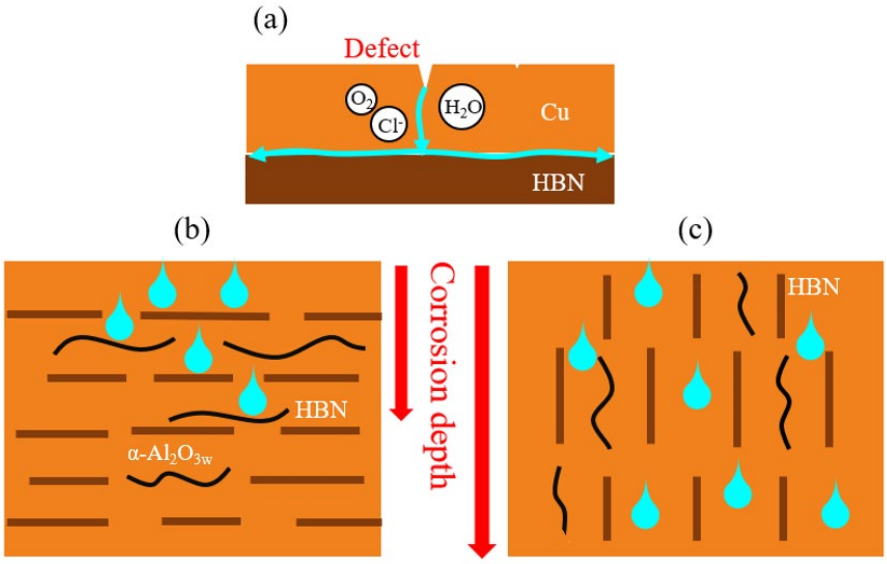

Fig. 13 Laminated composites (a) corrosion path; schematic of (b) corrosion depth vertical to laminated direction; (c) corrosion depth parallel to laminated direction

Conclusion

In this study, HBN-α-Al_2O_{3w} hybridized reinforced copper matrix composites with laminated structure were successfully prepared using FPM and vacuum hot press sintering. The effects of HBN content and ply structure on the mechanical and corrosion properties of the composites were investigated. Based on experimental results following conclusions can be drawn:

- It was found that ball milling of spherical Cu powder for 6 hours at a ball to

material ratio of 20:1 and a rotational speed of 300 rpm resulted in Cu flakes with the largest aspect ratio. The Cu flakes with a larger aspect ratio increase contact area with reinforcement, which improves density of composites and provides a basis for obtaining laminated structure.

- The surfaces of composites prepared by FPM showed a clear laminated distribution, but α-Al_2O_{3w} showed a more pronounced laminated distribution due to the special fiber structure. The XRD results of powders and blocks show that the addition of HBN leads to grain refinement.
- With the increase of HBN content, the strength of composites improves. However, the density of composites decreases due to agglomeration of reinforcement. Compared with non-laminated composites, laminated composites obtained higher densities. The laminated structure brings about crack deflection and improves the toughness of material. At the same time， pullout and fracture of the reinforcement improves the strength of composites. The combination of multiple reinforcement and toughening mechanisms achieves a balance between strength and toughness of composites.
- HBN can act as a good barrier layer to reduce contact between solution and matrix. The electrochemical results showed that composites with laminated structure enhanced surface flatness and reduced defects compared with non-laminated composites. At the same time, the special laminated structure makes matrix have a better diverting effect on corrosive liquid perpendicular to laminated direction, preventing the corrosion from developing to the inside. Therefore, the corrosion

resistance of laminated composites perpendicular to laminated direction is better than parallel direction.

References

[1] Z. Hussain, H. Jang, H. Choi, B.S. Choi, Microstructure, Mechanical Behavior, and Thermal Conductivity of Three-Dimensionally Interconnected Hexagonal Boron Nitride-Reinforced Cu-Ni Composite, J. Mater. Eng. Perform., 2021, 31, p 2792-2800.

[2] Q. Liu, Y. Liu, S.W. Tang, J.J. Cheng, Y.M. Chen, F. Wang, Z. Lv, X.H. Qu, Effects of Morphological Characteristics of Graphite Fillers on the Thermal Conductivity of the Graphite/Copper Composites Fabricated by Vacuum Hot pressing sintering, Vacuum, 2019, 167, p 199-206.

[3] P. Gao, Z.X. Liu, B. Tian, Y.X. Tong, F. Chen, L. Li, Microstructure, Phase Transformation and Mechanical Properties of NiMnGa Particles/Cu Composites Fabricated by SPS, T. Nonferr. Metal. Soc., 2022, 32, p 3291-3300.

[4] L.L. Meng, X.J. Wang, J.L. Ning, X.S. Hu, G.H. Fan, K. Wu, Beyond the Dimensional Limitation in Bio-Inspired Composite: Insertion of Carbon Nanotubes Induced Laminated Cu Composite and the Simultaneously Enhanced Strength and Toughness, Carbon, 2018, 130, p 222-232.

[5] R. Shu, X.S. Jiang, H.L. Sun, Z.Y. Shao, T.F. Song, Z.P. Luo. Recent Researches of the Bio-Ispired Nano-Carbon Reinforced Metal Matrix Composites. Compos.

Part A-Appl. S., 2020, 131, p 105816.

[6] F. Luo, X.S. Jiang, W.Y. Tan, H.L. Sun, Y.L. Zhang, Y.J. Fang, R. Shu, H.C. Cheng, Microstructures and Mechanical Properties of α-Al_2O_{3w} and MWCNTs Hybrid Reinforced Laminated Cu Matrix Composites, Compos. Interface., 2022, 30, p 341-360.

[7] W.Y. Tan, X.S. Jiang, Z.Y. Shao, H.L. Sun, T.F. Song, Z.P. Luo, Fabrication and Mechanical Properties of α-Al_2O_3 Whisker Reinforced Cu-Graphite Matrix Composites, Powder Technol., 2020, 375, p 124-135.

[8] C.Y. Liu, X.S. Jiang, H.L. Sun, Y.L. Zhang, Y.J. Fang, R. Shu, Microstructure and Mechanical Properties of Bioinspired Laminated CoCrFeNiMn High Entropy Alloy Matrix Composites Reinforced with Graphene, Mat. Sci. Eng. A-Struct., 2022, 859, p 144198.

[9] Z.J. Hu, R.F. Guo, S.M. Chen, Q. Jin, P. Shen, Synthesis of Damage-Tolerant Cu-Matrix Composites with Nacre-Inspired Laminate-Reticular Hierarchical Architecture Via Tuning Compositional Wettability, Scripta Mater., 2020, 186, p 312-316.

[10] H. Wei, Z. Li, D.B. Xiong, Z. Tan, G. Fan, Z. Qin, D. Zhang, Towards Strong and Stiff Carbon Nanotube-Reinforced High-Strength Aluminum Alloy Composites Through a Microlaminated Architecture Design, Scripta Mater., 2014, 75, p 30-33.

[11] J.W. Wu, X.H. Tang, X.M. Zhang, X. Cen, B.S. Guo, B.A. Chen, W. Li, Z.G. Zhang, Realizing the Combination of High Strength and Good Ductility of Cu

Matrix Composites with CrCoNi Reinforcement Particles and Microlaminated Structure, J. Alloy Compd., 2021, 872, p 159632.

[12] K. Zhang, G.S. Shao, W. Li, X.H. Chen, F.C. Ma, P. Liu, Wear and Corrosion Behavior of Graphene-Nanoplate-Reinforced Copper Matrix Composites Prepared Through Electrostatic Self-Assembly, J. Mater. Eng. Perform., 2019, 28, p 1650-1660.

[13] D.B. Xiong, M. Cao, Q. Guo, Z.Q. Tan, G.L. Fan, Z.Q. Li, Q. Zhang, Graphene-and-Copper Artificial Nacre Fabricated by a Preform Impregnation Process: Bioinspired Strategy for Strengthening Toughening of Metal Matrix Composite, Acs Nano, 2015, 9, p 6934-6943.

[14] C.J. Huang, J.S. Peng, Y.R. Cheng, Q. Zhao, Y. Du, S.X. Dou, A.P. Tomsia, H.D. Wagner, L. Jiang, Q.F. Cheng, Ultratough Nacre-Inspired Epoxy-Graphene Composites with Shape Memory Properties, J. Mater. Chem. A, 2019, 7, p 2787-2794.

[15] L. Jiang, G.L. Fan, Z.Q. Li, X.Z. Kai, D. Zhang, Z.X. Chen, S. Humphries, G. Heness, W.Y. Yeung, An Approach to the Uniform Dispersion of a High-Volume Fraction of Carbon Nanotubes in Aluminum Powder, Carbon, 2011, 49, p 1965-1971.

[16] J. Corrochano, C. Cerecedo, V. Valcarcel, M. Lieblich, F. Guitian, Whiskers of α-Al_2O_3 as Reinforcement of a Powder Metallurgical 6061 Aluminum Matrix Composite, Mater. Lett., 2008, 62, p 103-105.

[17] Y. Zhong, H. Chen, W. Hu, G. Gottstein, Fiber Damage and High Temperature

Tensile Properties of Al_2O_3 Fiber Reinforced NiAl-Matrix Composites with and without hBN-Interlayer, Mat. Sci. Eng. A-Struct., 2007, 464, p 241-248.

[18] X.Y. Wen, R. Joshi, 2D Materials-Based Metal Matrix Composites, J. Phys. D Appl. Phys., 2020, 53, p 423001.

[19] K.L. Zhang, Y.L. Feng, F. Wang, Z.C. Yang, J. Wang, Two-Dimensional Hexagonal Boron Nitride (2D-hBN): Synthesis, Properties and Applications, J. Mate. Chem. C, 2017, 5, p 11992-12022.

[20] J.G. Wang, F.C. Ma, M.T. Sun, Graphene, Hexagonal Boron Nitride, and Their Heterostructures: Properties and Applications, Rsc Adv., 2017, 7, p 16801-16822.

[21] J. Bao, K. Jeppson, M. Edwards, Y.F. Fu, L.L. Ye, X.Z. Lu, J. Liu, Synthesis and Applications of Two-Dimensional Hexagonal Boron Nitride in Electronics Manufacturing, Electron. Mater. Lett., 2016, 12, p 1-16.

[22] T. Natsuki, J. Natsuki, Prediction of Mechanical Properties for Hexagonal Boron Nitride Nanosheets Using Molecular Mechanic Model, Appl. Phys. A-Mater., 2017, 123, p 283.

[23] R. Tyagi, D.S. Xiong, J.L. Li, J.H. Dai, High-Temperature Friction and Wear of Ag/h-BN-Containing Ni-Based Composites Against Steel, Tribol. Lett., 2010, 40, p 181-186.

[24] A. El-Tantawy, W.M. Daoush, A.E. El-Nikhaily, Microstructure and Properties of BN/Ni-Cu Composites Fabricated by Powder Technology. J. Exp. Nanosci., 2018, 13, p 174-187.

[25] Z. Hussain, H. Jang, H. Choi, B.S. Choi, Microstructure, Mechanical Behavior,

and Thermal Conductivity of Three-Dimensionally Interconnected Hexagonal Boron Nitride-Reinforced Cu-Ni Composite, J. Mater. Eng. Perform., 2022, 31, p 2792-2800.

[26] J. Zhang, Y.C. Yang, J. Lou, Investigation of Hexagonal Boron Nitride as an Atomically Thin Corrosion Passivation Coating in Aqueous Solution, Nanotechnology, 2016, 27, p 364004.

[27] J.H. Hwang, B.K. Shrestha, J.H. Kim, T.H. Seo, C.H. Park, M.J. Kim, Nanoscale Layer of a Minimized Defect Area of Graphene and Hexagonal Boron Nitride on Copper for Excellent Anti-Corrosion Activity, Nanotechnology, 2022, 33, p 055601.

[28] G.H. Zhang, X.S. Jiang, C.J. Qiao, Z.Y. Shao, D.G. Zhu, M.H. Zhu, V. Valcarcel, Investigation of the Microstructure and Mechanical Properties of Copper-Graphite Composites Reinforced with Single-Crystal α-Al_2O_3 Fibers by Hot Isostatic Pressing, Materials, 2018, 11, p 982–1000.

[29] R. Shu, X.S Jiang, Z.Y. Shao, D.M. Sun, D.G. Zhu, Z.P. Luo, Fabrication and Mechanical Properties of MWCNTs and Graphene Synergetically Reinforced Cu-Graphite Matrix Composites, Powder Technol., 2019, 349, p 59-69.

[30] X. Wang, X.S. Jiang, H.L. Sun, Z.Y. Shao, Y.L. Zhang, Y.J. Fang, R. Shu, Influence of Ratio of Multi-Walled Carbon Nanotubes and Graphene on Microstructure and Mechanical Properties of Copper-Graphite Composites Fabricated by Spark Plasma Sintering, Compos. Interface., 2022, 29, p 1267-1287.

[31] Z.Y. Shao, H.K. Pan, R. Shu, X.S. Jiang, M.H. Zhu, Microstructures and Interfacial Interactions of Al_2O_3 Whiskers and Graphene Nano-Platelets Co-Reinforced Copper Matrix Composites, T. Nonferr. Metal. Soc., 2022, 32, p 2935-2947.

[32] G.H. Zhang, X.S. Jiang, Z.Y. Shao, H.L. Sun, Q. Ma, Z.P. Luo, Microstructures and Mechanical Properties of Alumina Whisker Reinforced Copper Matrix Composites Prepared by Hot-Pressing and Hot Isostatic Pressing, Mater. Res. Express, 2019, 6, p 116513.

[33] W.Y. Tan, X.S. Jiang, Z.Y. Shao, H.L. Sun, Y.J. Fang, R. Shu, Fabrication and Mechanical Properties of Nano-Carbon Reinforced Laminated Cu Matrix Composites, Powder Technol., 2022, 395, p 377-390.

[34] Z. Li, Q. Guo, Z.Q. Li, G.L. Fan, D.B. Xiong, Y.S. Su, J. Zhang, D. Zhang, Enhanced Mechanical Properties of Graphene (Reduced Graphene Oxide)/Aluminum Composites with a Bioinspired Nano-Laminated Structure, Nano Letters., 2015, 15, p 8077-8083.

[35] W.T. Huo, C.X. Lei, Y. Du, G. Chang, M. Zhu, B. Chen, Y.S. Zhang, Superior Strength-Ductility Synergy of (TiC + Ti5Si3)/Ti Composites with Nacre-Inspired Architecture, Compos. Part B-Eng., 2020, 240, p 109991.

[36] X.Z. Wang, Y.S. Su, Q.B. Ouyang, C.N. Zhu, H. Cao, D. Zhang, Fabrication, Mechanical and Thermal Properties of Copper Coated Graphite Films Reinforced Copper Matrix Laminated Composites Via Ultrasonic-Assisted Electroless Plating and Vacuum Hot-Pressing Sintering, Mat. Sci. Eng. A-Struct., 2021, 824,

p 141768.

[37] M. Zhao, D.B. Xiong, Z.Q. Tan, G.L. Fan, Q. Guo, C.P. Guo, Z.Q. Li, D. Zhang, Lateral Size Effect of Graphene on Mechanical Properties of Aluminum Matrix Nano-Laminated Composites, Scripta Mater., 2017, 139, p 44-48.

[38] S.J. Yuan, S.O. Pehkonen, Surface Characterization and Corrosion Behavior of 70/30 Cu-Ni Alloy in Pristine and Sulfide-Containing Simulated Seawater, Corros. Sci., 2007, 49, p 1276-1304.

[39] X.H. Chen, P.Z. Liu, P. Liu, H.H. Chen, Preparation of Copper-Graphene Layered Composites by Spark Plasma Sintering, Mater. Sci. Tech-Lond., 2018, 34, p 1693-1699.

[40] J. Wang, L.N. Guo, W.M. Lin, J. Chen, S. Zhang, S.D. Chen, T.T. Zhen, Y.Y. Zhang, The Effects of Graphene Content on the Corrosion Resistance, and Electrical, Thermal and Mechanical Properties of Graphene/Copper Composites, New Carbon Mater., 2019, 34, p 161-169.

[41] J.B. Jorcin, M.E. Orazem, N. Pebere, B. Tribollet, CPE Analysis by Local Electrochemical Impedance Spectroscopy, Electrochim. Acta, 2006, 51, p 1473-1479.

[42] C.C. Pan, X. Zhang, F. Yang, D.H. Xia, C.N. He, W.B. Hu, Corrosion and Cavitation Erosion Behavior of GLNN/Cu Composite in Simulated Seawater, Acta Metall. Sin., 2022, 58, p 599-609.

[43] A. Shaga, S. Ping, L.G. Xiao, R.F. Guo, Y.B. Liu, Q.C. Jiang, High Damage-Tolerance Bio-Inspired ZL205A/SiC Composites with a Lamellar-Interpenetrated

Structure, Mat. Sci. Eng. A-Struct., 2017, 708, p 199–207.

[44] P. Madhukar, N. Selvaraj, G.B.V. Kumar, C.S.P. Rao, F. Mohammad, M. Chavali, Effect of TiC_{np} on Microstructure and Mechanical Behavior of High-Properties Al7150-TiC Nanocomposites, Mat. Sci. Eng. B-adv., 2012, 265, p 115034.

[45] M. Yang, L. Weng, H.X. Zhu, F. Zhang, T.X. Fan, D. Zhang, Leaf-Like Carbon Nanotube Graphene Nanoribbon Hybrid reinforcement for Enhanced Load Transfer in Copper Matrix Composites, Scripta Mater., 2017, 138, p 17–21.

[46] S. Cui, C.X. Cui, J. Lv, S.Y. Chen, J.Q. Xie, S.J. Liu, Fabrication, Microstructure and Mechanical Properties of Al_2O_3 Whiskers Reinforced Ti-46Al-4Nb Alloy, Mater. Lett., 2020, 259, p 126902.

[47] F. Long, X.H. Guo, K.X. Song, J.Q. Liu, X. Wang, Y.B. Yang, S.L. Li, An Internal-Oxidation Based Strategy Induced High-Density Alumina In-Situ Nanoprecipitation and Carbon Nanotube Interface Optimization for Co-Reinforcing Copper Matrix Composites, Compos. B Eng., 2022, 229, p 109455.

[48] K.W. Fan, F.M. Zhang, C.Y. Shang, F. Saba, J. Yu, Mechanical Properties and Strengthening Mechanisms of Titanium Matrix Nanocomposites Reinforced with Onion-Like Carbons, Compos. Part A-Appl. S., 2020, 132, p 105834.

[49] W.J. Xia, J.Q. Song, Z.X. Meng, C. Shao, S. Keten, Designing Multi-Layer Graphene-Based Assemblies for Enhanced Toughness in Nacre-Inspired Nanocomposites, Mol. Syst. Des. Eng., 2016, 1, p 40–47.

[50] T. Aben, D. Tromans, Anodic Polarization Behavior of Copper in Aqueous Bromide and Bromide/Benzotriazole Solutions, J. Electrochem. Soc., 1995, 142,

p 398-404.

[51] I. Milošev, N. Kovačević, J. Kovač, A. Kokalj, The Roles of Mercapto, Benzene and Methyl Groups in the Corrosion Inhibition of Imidazoles on Copper: I. Experimental Characterization, Corros. Sci., 2015, 98, p 107-118.

[52] X.N. Liao, F.H. Cao, L.Y. Zheng, W.J. Liu, A.N. Chen, J.Q. Zhang, C.A. Cao, Corrosion Behavior of Copper Under Chloride-Containing Thin Electrolyte Layer, Corros. Sci. 2011, 53, p 3289–3298.

[53] A. Jamwal, P. Prakash, D. Kumar, N. Singh, K.K. Sadasivuni, K. Harshit, S. Gupta, P. Gupta, Microstructure, Wear and Corrosion Characteristics of Cu Matrix Reinforced SiC-Graphite Hybrid Composites, J. Compos. Mater., 2019, 53, p 2545-2553.

[54] Y.M. Xie, X.C. Meng, D.X. Mao, Z.W. Qin, L. Wan, Y.X. Huang, Homogeneously Dispersed Graphene Nanoplatelets as Long-Term Corrosion Inhibitors for Aluminum Matrix Composites, ACS Appl. Mater. Interfaces, 2021, 13, p 32161–32174.

[55] B.Y. Jin, D.B. Xiong, Z.Q. Tan, G.L. Fan, Q. Guo, Y.S. Su, Z.Q. Li, D. Zhang, Enhanced Corrosion Resistance in Metal Matrix Composites Assembled from Graphene Encapsulated Copper Nanoflakes, Carbon, 2019, 142, p 482-490.